

Direct observations of Pd–Te compound formation within noble metal inclusions in spent nuclear fuel

Sean H. Kessler, Timothy G. Lach, Kerry E. Garrett, Michele A. Conroy¹,
David G. Abrecht, Jon M. Schwantes, Richard A. Clark^{*}

Pacific Northwest National Laboratory, 902 Battelle Boulevard, Richland, WA, 99352, USA

HIGHLIGHTS

- Nanoscale chemical segregation of Pd from the other noble metal phase (NMP) elements in UO₂ fuels has been observed.
- Detailed elemental analysis reveals the presence of a Te-rich secondary phase within NMP particles.
- Ab-initio chemical computations support the conclusion that the telluride phase drives fractionation of Pd and Ru.
- Results have implications for both the formation mechanism of NMP particles and their behavior in waste repositories.

ARTICLE INFO

Article history:

Received 21 September 2019

Received in revised form

15 May 2020

Accepted 16 May 2020

Available online 28 May 2020

Keywords:

Transition metal alloys and compounds

Noble metal phase particles

Nuclear reactor materials

Thermodynamic modeling

Palladium telluride

ABSTRACT

Although the existence of a five-metal (Mo–Tc–Ru–Rh–Pd) phase – as nanoparticles observed in irradiated nuclear fuel – has been known for more than half a century, the chemical and physical mechanisms controlling the formation and behavior of such particles remain stubbornly elusive. We present in this work new evidence for the presence of a separate nonmetallic phase associated with the metallic particles and containing a significant fraction of Te in addition to Pd. While this new phase potentially complicates the thermodynamic picture of a mixed alloy in equilibrium with the surrounding fuel environment, it also provides new clues in the search for a chemical mechanism for Pd migration through the uranium dioxide matrix and the nucleation behavior of the particles. Fractionation between phases may subsequently affect the mechanical performance of fuels during irradiation and their interactions with the surrounding environment during long-term waste storage.

© 2020 The Authors. Published by Elsevier B.V. This is an open access article under the CC BY-NC-ND license (<http://creativecommons.org/licenses/by-nc-nd/4.0/>).

1. Introduction

Typical light water reactor (LWR) fuels consisting of either uranium oxide, UO₂, or mixed oxide, (Pu_xU_{1-x})O₂, rapidly produce a wide range of fission products during irradiation, many of which aggregate into new phases distinct from the initial actinide oxide. Some products have a sufficiently low oxidation potential to form additional oxide phases (or remain in the actinide oxide matrix), others exist as volatile species, and another group—consisting primarily of the high-yield fission products Mo, Tc, Ru, Rh, and Pd—has been observed to exist as metallic nanoparticles [1]. These particles, which are often observed along grain boundaries in the

fuel, can range from small nuclei of a few nanometers to micron-sized aggregates [2,3]. Because of the significant amount of ruthenium observed in these inclusions, the associated alloy is most likely to exist at thermodynamic equilibrium with a hexagonally close-packed (hcp) ϵ -phase structure [4,5]. This phase has gone by several names in the literature, including white inclusions [1,6], fission product alloy [1], 5-metal particles [7], ϵ -phase particles [8,9], and noble metal phase [5,10]. Although recent studies have cast some uncertainty on both the degree of crystallinity [3] and the single-phase metallic nature (this work) of the inclusions, we will continue to refer to them as noble metal phase (NMP) particles for the sake of convenience and continuity.

One reason for the interest in better understanding the properties of NMP particles is their mechanical effects on the fuel matrix as they form during irradiation. Many of the larger particles have been observed along grain boundaries of UO₂ [3], and their growth could potentially lead to swelling of the fuel pellet or change the

^{*} Corresponding author.

E-mail address: Richard.Clark@pnnl.gov (R.A. Clark).

¹ Present Addresses: University of Limerick, Limerick, V94 T9PX, Ireland.

brittleness of the surrounding material [11]. Additionally, recent experiments have demonstrated that extracted particles suspended in aqueous solution of other spent fuel components can contribute catalytically to the reduction of actinides and thereby promote immobilization of the waste form [12]. Consequently, greater understanding of the formation mechanism, size distribution, and chemical state of the particles is essential to better predicting these secondary effects on spent fuel behavior.

To date, much of the theoretical work of describing the NMP has focused on the thermodynamics of mixing in the metal alloy. This has included both CALPHAD techniques, which employ consistent descriptions of the free energy of all binary (and some ternary) combinations of the constituent elements [5,13–15], and *ab initio* explorations of the substitutionally disordered metal for key subsets of the full quinary system [16–21]. These thermodynamic approaches are employed to predict the fractionation of elements between phases; it is crucial to note in such cases that because migration through the fuel is limited by low diffusion rates, equilibrium often can only be said to exist locally at very small scales (from nm to μm), rather than for the fuel pellet as a whole.

Although the NMP contains a significant fraction of the noble metal fission products [22], additional phases have been investigated as competing chemical forms, including MoO_2 [10,23] and the Pd–Te intermetallic system [24–26]. Equilibrium fractionation between phases is controlled by the oxidation potential of the immediate fuel environment and can lead to variations in the observed composition of a given NMP particle. At the same time, other elements besides the five noble metals have been identified in the particles, including trace amounts of U [3] and up to 6 at.% Te [2,27]. The observation of significant amounts of Te has been supported by recent studies of residues from fuel dissolution [3,22], but the chemical form of the Te has previously been approached as that of a metal incorporated directly into the alloy. The evidence presented in this work suggests that the actual microstructure of the particle consists of two or more phases, comprising both the Ru-rich hcp metal and a Pd-rich telluride structure.

2. Methods

2.1. Electron microscopy

The NMP particles included in this study originated from the high-burnup fuel sample designated Approved Test Material 109 (ATM-109) [28]. This UO_2 fuel had an initial enrichment of 3.0% ^{235}U and was irradiated in a boiling water reactor (BWR) to a total cumulative burn-up of $70.80 \text{ GWd MTU}^{-1}$ [3]. A segment of the post-irradiation fuel was removed from the cladding at PNNL for dissolution experiments [3,22], and the remaining portion of cladding was examined for residues of uranium oxide and fission products [29].

Sections of the zirconium oxide layer of the fuel-cladding interface region were examined with scanning electron microscopy (SEM) using the FEI Helios NanoLab 660 dual-beam focused ion beam/scanning electron microscope (FIB/SEM) [29]. Cross-sections of this layer, measuring $\sim 10 \mu\text{m}$ long and $\sim 10 \mu\text{m}$ deep, were removed using standard TEM lift-out techniques; final thinning was performed at low energy (2 kV) to remove any Ga-ion beam damage from the FIB [30]. The lift-out was characterized by scanning transmission electron microscopy (STEM) on the JEOL ARM200CF aberration-corrected microscope and large diameter SDD energy dispersive spectroscopy (EDS) detector. Detailed characterization of the zirconium oxide layer, including phase and grain size distribution, were conducted by Lach et al. [31], and characterization of the particle and void distribution in this same layer were conducted by Clark et al. [29] and Schwantes et al. [32].

Fig. 1 shows a STEM high-angle annular dark field (HAADF) image of the FIB liftout used for the analysis in this work. The numerous bright white spots in the image were identified as containing noble metal fission products, two of which were studied at high magnification for elemental composition. These two NMP particles are labelled in Fig. 1 as points A and B. The first is a non-spherical particle much larger than the other particles in the image (with an approximate diameter of 200 nm) and appears to have formed as an agglomeration of smaller particles. The second particle is smooth and slightly oblong, with a minor axis width of 50 nm and a major axis of 67 nm.

2.2. Computational thermodynamics

The free energies of the substitutionally disordered metallic alloy phase and the proposed telluride phase were examined using the cluster expansion formalism, also sometimes referred to as the Connolly-Williams (CW) approach, in which the energy of a configuration of atoms on a fixed crystal lattice is expressed as a linear combination of cluster interactions [33,34]:

$$E(\sigma) = \sum_{\alpha} Q_{\alpha} J_{\alpha} \xi_{\alpha}(\sigma) = \sum_{\alpha} \left[Q_{\alpha} J_{\alpha} \left\langle \prod_{i \in \alpha} \sigma_i \right\rangle \right], \quad (1)$$

where α represents the index of each symmetrically irreducible cluster, Q_{α} is the degeneracy of the cluster (i.e. the number of symmetrically equivalent instances of the cluster per unit cell), and $\xi_{\alpha}(\sigma)$ is the correlation function, which for a binary alloy system can be expressed simply as the product of effective Ising spins of the atoms at each lattice point, averaged over all symmetrically equivalent clusters. For all applications in this paper, we adopt the convention $\sigma_{\text{Ru}} = +1$ and $\sigma_{\text{Pd}} = -1$. Lastly, the term J_{α} is typically called the effective cluster interaction (ECI) and describes the energy associated with each cluster set in the expansion.

In theory, a cluster expansion that extends over all possible combinations (including fourth- and higher-order clusters and long-range interactions) can describe exactly the energy of any given configuration of atoms on a lattice. The practical utility of the CW method arises from the observation that only a handful of short-range interactions, typically third-order or lower, are

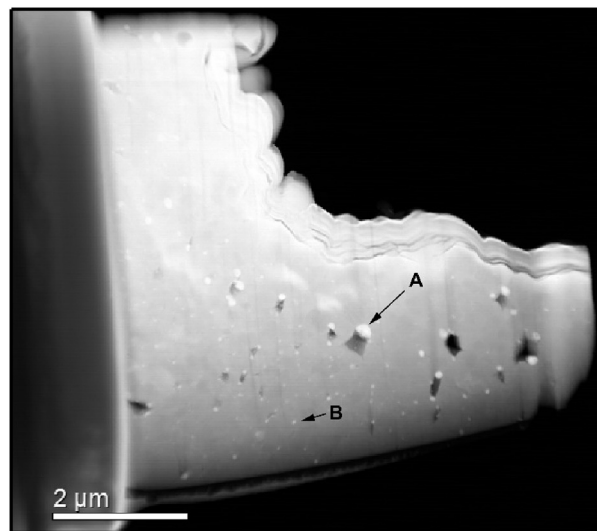


Fig. 1. STEM-HAADF image of a FIB liftout of a section of zirconia from the cladding of ATM-109 fuel. White inclusions are identified as NMP particles, with the specific particles examined in Figs. 3 and 4 labelled here as points A and B, respectively.

necessary to describe the energy with adequate accuracy; errors in estimating the formation energy tend to be on the order of a few meV. Obtaining the ECIs for these short-range terms most frequently entails performing *ab initio* calculations of the energy of formation for a limited training set (40–50 structures), followed by inverting Eq. (1) through linear regression to obtain the values $\{J_\alpha\}$ that minimize the sum-of-squares error (10–20 ECIs in most cases) [35,36].

The metallic phases of interest in the binary alloy system are the Pd-rich fcc α phase and the Ru-rich hcp ϵ phase. For each phase, fifty structures were selected spanning the full range of concentration, from pure Pd to pure Ru, using the ATAT software package [35–37]. The unit cells used for the fcc phase included one to five atoms, depending on the structure, and the hcp unit cells contained two to six atoms. Two palladium telluride structures were also selected to probe the mixing thermodynamics of the nonmetallic phases in the system: PdTe and Pd₂₀Te₇ [38,39], which are depicted in Fig. 2c and d, respectively. Although the Pd–Te phase diagram shows that there are several other intermetallic compounds that could conceivably form in this system [26], the two selected bookend the approximate range of atomic Pd/Te ratios that have been observed previously and make a suitable base case for exploring the energetics of incorporating ruthenium into the telluride system [2,22,27,29]. Both structures belong to the hexagonal crystal family, along with the hcp metal phase, and they are stable up to their relevant melting temperatures. The CW approach is used for the pseudobinary systems by applying the cluster correlation functions $\xi_\alpha(\sigma)$ to the arrangement of Pd and Ru atoms on the Pd sublattice, leaving the Te sublattice untouched.

The incorporation of Ru into the Pd–Te phases is simulated through direct substitution onto the Pd sublattice of the initial crystal structure. For the PdTe crystal structure, fifty different compounds were again selected using the ATAT software package [35,37] with the empirical formula (Pd_{1-x}Ru_x)Te, where $0 \leq x \leq 1$. For the Pd₂₀Te₇ structure, compounds were selected by replacing either one or two Pd atoms on the lattice with a corresponding Ru atom, covering all possible combinations within one unit cell such that the composition range $0 \leq x \leq 0.1$ is studied. Because the energy of formation is observed to be strongly unfavorable for even small concentrations of Ru, values beyond this range were deemed

unnecessary for the analysis.

Ground-state energies for all structures, used to fit Equation (1) for ECI values, were calculated using the Vienna *Ab-initio* Simulation Package (VASP) [40,41] with the projector augmented-wave (PAW) method and the energy functional approximation of Perdew, Burke, and Ernzerhof (PBE) [42,43]. A plane-wave cutoff energy of 350 eV was used for all calculations. Electronic structure calculations used a convergence criterion of 1×10^{-7} eV, and ionic positions and cell parameters were relaxed until all Hellman-Feynman forces on all atoms had magnitudes less than 5×10^{-3} eV Å⁻¹. K-point meshes were selected by scanning different sizes of Monkhorst-Pack mesh for end-member compounds in each system until energy discrepancies were less than 1 meV for each simulation [44]. A $15 \times 15 \times 15$ mesh was used for the fcc, hcp, and PdTe structures, and a $7 \times 7 \times 7$ mesh was used for the Pd₂₀Te₇ system.

Phonon calculations for the Pd–Ru–Te system described here were originally performed for the binary alloy phases and the Pd–Te phase. However, these calculations displayed no clear trend in the vibrational entropy of formation of the compounds and tended to have only a very small effect on the final results. These have been omitted from the reported work for clarity. Moreover, we have observed in our previous work [20] and that of others [45] that vibrational contributions to the entropy of formation in alloys tend to be very small except in some select cases which involve a bcc metal incorporated into a close-packed crystal lattice.

3. Results and discussion

3.1. Particle microstructure

The particle labelled by point A in Fig. 1 is examined at higher magnification in Fig. 3, covering an area of approximately 100 nm on each side. Heterogeneity in the particle, evidenced by intensity variations in the Z-contrast HAADF image (Fig. 3a), is supported further by the elemental EDS maps. The Ru, Mo, Tc, and Rh distribution represented in Fig. 3 shows regions of high concentration toward the top-left and bottom areas, while the Pd distribution has the highest concentration along the left and right sides of the image connected by a strip elevated in Pd and Te. The latter case correlates with the Te map (Fig. 3d), which qualitatively replicates the features of the Pd map. The anticorrelation between Ru and Pd is also better illustrated by Fig. 3i, which overlays the two individual maps with very little direct overlap. Elemental maps of Mo, Tc, and Rh also match approximately the Ru distribution, albeit with a weaker overall signal. Because the observed trend is strongest among Ru, Pd, and Te, the remainder of the results described here will focus on these three elements.

A quantitative measure of the variations in constituent elements across different regions of the particle is obtained from a line scan of the EDS spectra, depicted by a vertical arrow in Fig. 3. The resulting values are plotted in Fig. 3j, as a fraction of total EDS counts from all elements in the spectra. While Mo, Tc, and Rh do follow similar trends to the Ru, they were removed from this plot for clarity purposes. Because a calibration was not performed with a reference material, the values given do not correlate directly to atomic fractions, but rather provide a description of the relative changes in each element. There is some background noise from Zr and O, but it is relatively minimal as denoted by the Zr distribution in Fig. 3d. The resulting plot shows that local maxima in Ru concentration correspond to local minima in both Pd and Te, and vice-versa.

The second particle, labelled by point B in Fig. 1 and depicted in an expanded view in Fig. 4, shows a similar separation between phases as the first particle, but to a less noticeable extent. Although

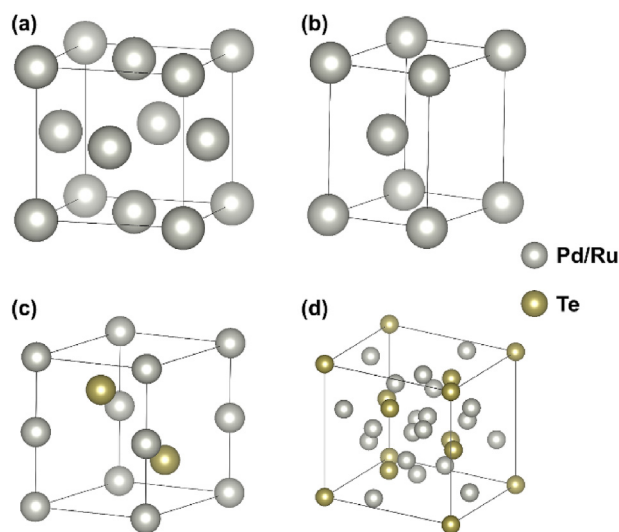


Fig. 2. Crystal structures of the (a) fcc and (b) hcp metallic phases studied in the Ru–Pd binary alloy system. (c) PdTe and (d) Pd₂₀Te₇ crystal structures used as the basis for studying substitutional ruthenium incorporation into the palladium telluride phase.

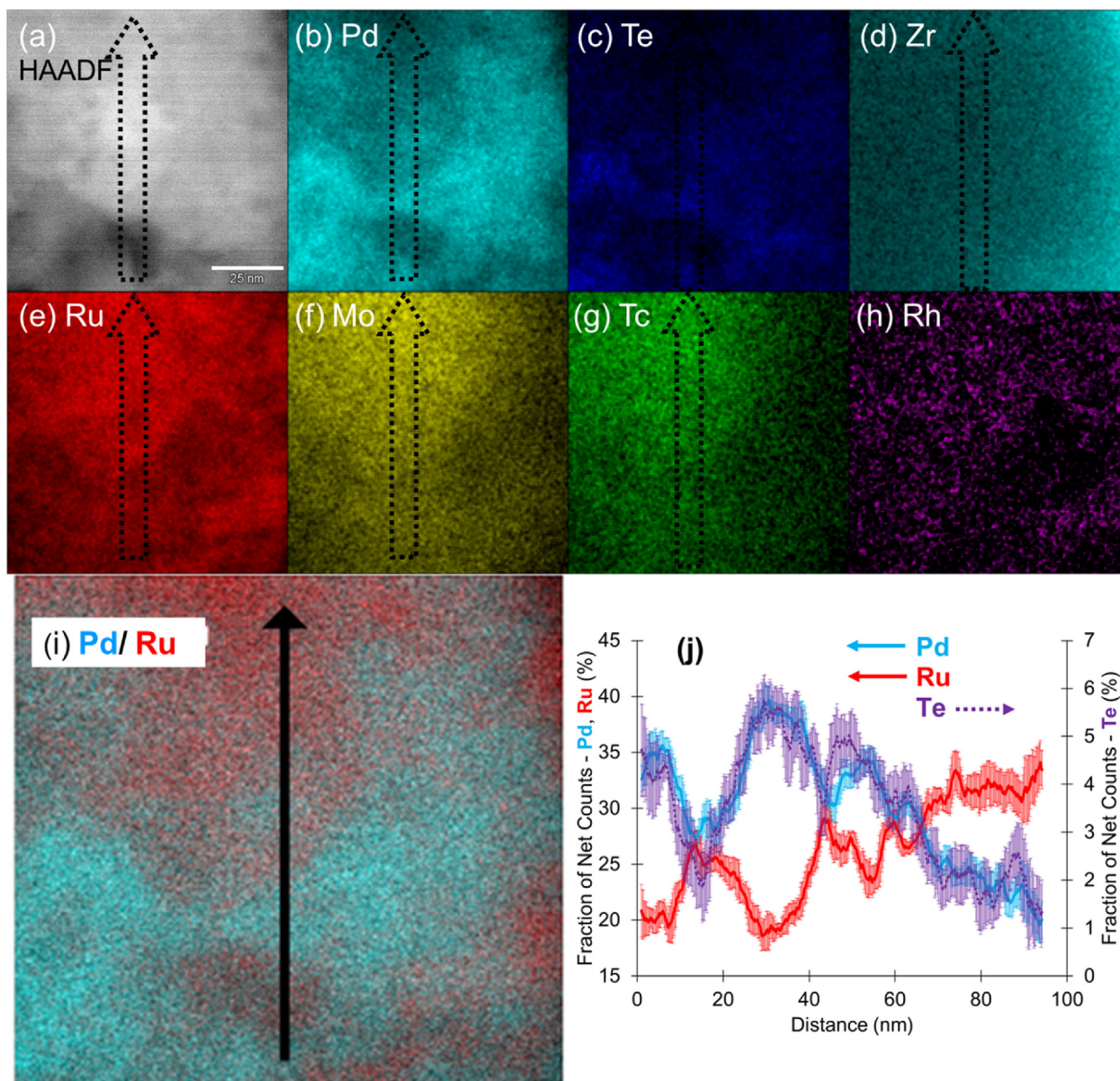


Fig. 3. (a) HAADF image of the interior area of the particle identified by point A in Fig. 1. EDS elemental maps of (b) Pd, (c) Te, (d) Zr, (e) Ru, (f) Mo, (g) Tc, and (h) Rh show varying ruthenium(molybdenum, technetium, rhodium)-rich and palladium/tellurium-rich regions throughout the image. (i) A combined Pd/Ru elemental map illustrating variations between the two phases, and an arrow indicating the path of a line scan of EDS values. (j) Fraction of EDS net count values of Ru, Pd, and Te across the path of the line scan, normalized by total elemental signal (including Zr, O, U, Tc, Rh, and Mo). Error bars represent one standard deviation.

the Ru elemental map (Fig. 4b) in this case covers the extent of the particle more or less evenly, there is a region of depleted Pd and Te (Fig. 4c and d) along the bottom edge of the particle, which appears between the 20- and 40-nm points in the line scan in Fig. 4f. Just as in Fig. 3, Mo, Tc, and Rh have similar distributions to that of the Ru. The apparent mixture of all three elements in the interior of the particle may be caused by having two separate phases overlapping each other in the given field of view, or the extent of phase separation as opposed to elemental mixing has not reached the high level found in larger particles in Fig. 3 and elsewhere [46]. In every particle analyzed (though not reported here; some included elsewhere [29,32]), this same behavior of two elemental segregation was observed with larger particles displaying a greater degree of separation. This was consistent as particles get even larger, phase separation continues to be more apparent as reported by Parrish

et al. [46]. Tomographic techniques, such as atom probe tomography (APT) [47], could provide a clearer picture of mixing and separation within the particle. APT was attempted, but, at this point, it has not provided useful data.

From the line scan in Fig. 3j, it is possible to obtain a quantitative picture of the degree of fractionation between the Ru-rich and Pd-rich phases. The ratio of Pd to Ru EDS counts at each averaged point is plotted against the Te:Ru ratio in Fig. 5, with error bars reflecting one standard deviation as taken from the average over every 2.0 nm. The data show a strong positive correlation, consistent with the qualitative observation that the Pd fractionation throughout the particle matches that of the Te. A linear fit of the data is likewise consistent with the linear mixing of two distinct phases, where said mixing occurs due to spatial averaging through the depth of the sample. The small nonzero intercept value indicates that a portion

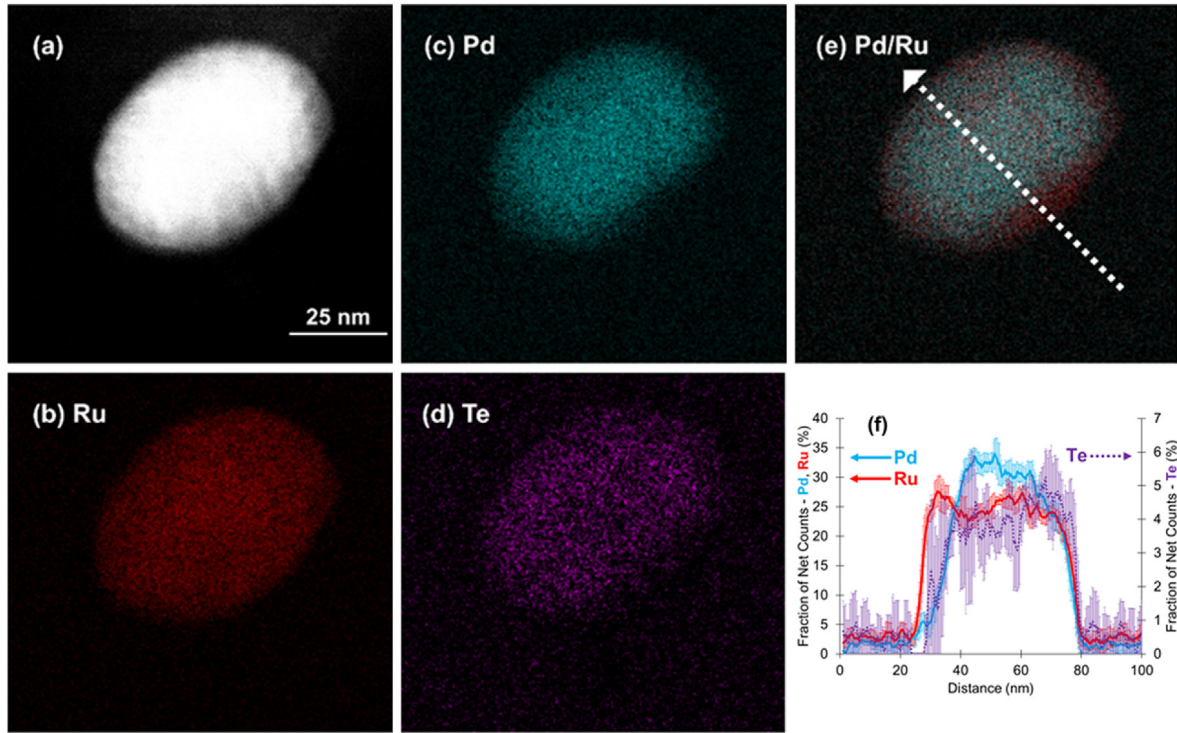


Fig. 4. (a) HAADF image of the particle identified by point B in Fig. 1. EDS elemental maps of (b) Ru, (c) Pd, and (d) Te indicate a small ruthenium-rich region near the bottom-right of the particle that is depleted in both palladium and tellurium. (e) A combined Ru/Pd elemental map illustrating the ruthenium-rich region more clearly, and a dashed arrow indicating the path of a line scan of EDS values across the minor axis of the particle. (f) Normalized elemental net count values of Ru, Pd, and Te across the path of the line scan. Error bars represent one standard deviation.

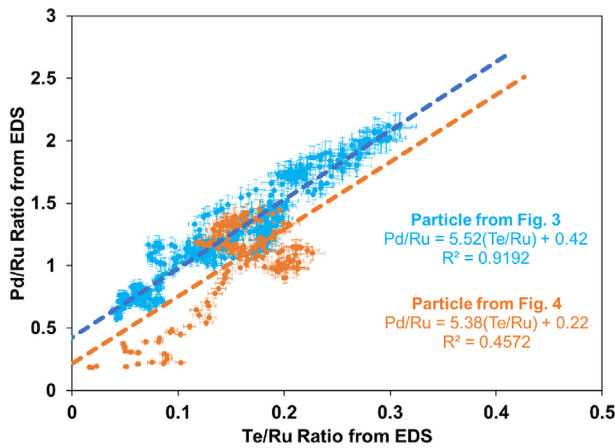


Fig. 5. Plot of the Pd/Ru ratio versus Te/Ru ratios taken from the line scan in Figs. 3j and 4f using the 2.0-nm spatially averaged values, with corresponding error bars at one standard deviation. The linear relationship between the values of Fig. 3 particle suggests simple mixing of two distinct phases. The linear fit to the data, depicted by a dashed line, returns a nonzero y-intercept, suggesting incomplete fractionation of Pd. In all particles analyzed which were > 100 nm, this same behavior was observed. Deviation from this linear fit was observed in most smaller particles. This could be due to overlapping phases in the field of view, or the phase separation not yet reaching a high level. See supplemental material for additional mixing line behavior for some other analyzed particles.

of the Pd remains in the metallic phase, although the concentration is still significantly higher in the telluride portion. This is further confirmed when looking at the mixing line from the smaller particle in Fig. 4. Qualitatively, there is more mixing of Pd, Te, and Ru in this particle than the larger particle; thus, it is reasonable that the

intercept value is closer to zero than the larger particle that visually has a great degree of phase separation. It is rational for the larger noble metal phase particles to have a greater Te content and thus greater phase separation and fractionation between Pd–Te and Ru, Mo, Tc, and Rh. Fractionation likely depends on the size of the noble metal phase particles. This mixing line behavior is found in other particles that have been analyzed as shown in the supplemental material.

3.2. Thermodynamic analysis

The strong fractionation of Pd between the metallic and telluride phases is further supported by the first-principles thermodynamic analysis of the corresponding systems. Fig. 6 displays the energies of formation for all four crystal structures outlined in Fig. 2, comprising 230 compounds in all. From the cluster expansion fits to this data, using Eq. (1), the substitutionally disordered energy of formation can be expressed simply as

$$\Delta E_f = \sum_n (2x_{Ru} - 1)^n J^{[n]}, \quad (2)$$

where x_{Ru} is the mole fraction of Ru on the Pd–Ru sublattice (i.e. not counting the Te in the system), n is the cluster order from 0 to 3, and $J^{[n]} = \sum_{\alpha \in n} Q_{\alpha} J_{\alpha}$ is the multiplicity-weighted sum of all ECI values with the same order of cluster. These combined ECI values are listed in Table 1 for all four crystal systems. Because the Pd₂₀Te₇ system only includes compositions up to $x_{Ru} = 0.1$, only the null and point clusters ($n = 0$ and $n = 1$) were used to fit that data set, which is sufficient to determine the initial slope of the energy in the limit of low Ru concentration.

From inspection of the energy of formation for the disordered system, it is apparent that the incorporation of Ru into a Pd-rich

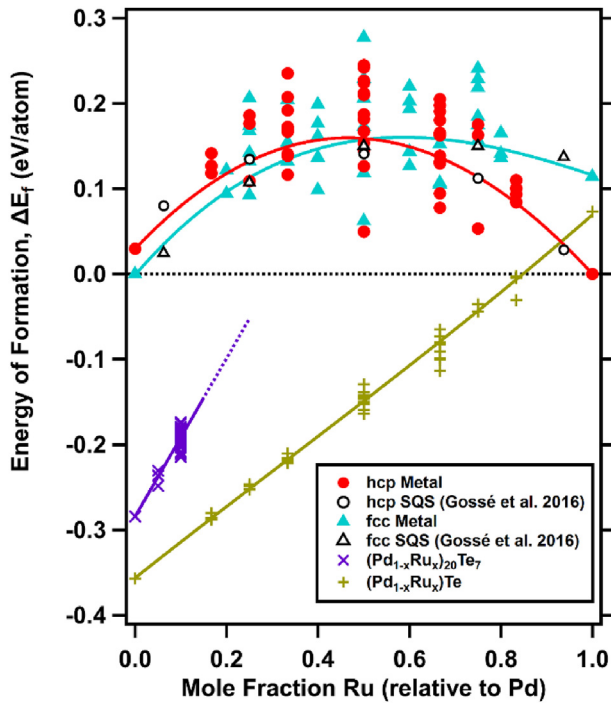


Fig. 6. DFT-calculated formation energies plotted against Ru composition in four selected phases: the binary hcp (red circles) and fcc (cyan triangles) alloy phases, as well as the $\text{Pd}_{20}\text{Te}_7$ (purple 'x' marks) and PdTe (yellow crosses) intermetallic compound. The latter compounds are treated as pseudobinary systems in which Ru is substituted for Pd atoms on the transition metal sublattice. Solid lines represent the disordered solid solution for each crystal structure as described by equation (1). Open circles and triangles represent special quasirandom structure (SQS) calculations for the hcp and fcc phases, respectively, taken from Gossé et al. [19]. (For interpretation of the references to colour in this figure legend, the reader is referred to the Web version of this article.)

Table 1
Combined effective cluster interaction values (eV atom^{-1}), reported to four decimal places, for the Pd–Ru sublattice of each of the four crystal systems depicted in Fig. 2.

	hcp Metal	fcc Metal	$(\text{Pd}_x\text{Ru}_{1-x})\text{Te}$	$(\text{Pd}_x\text{Ru}_{1-x})_{20}\text{Te}_7$
$J^{[0]}$	0.1588	0.1575	−0.1490	0.1795
$J^{[1]}$	−0.0198	0.0325	0.2074	0.4638
$J^{[2]}$	−0.1441	−0.1000	0.0055	—
$J^{[3]}$	0.0051	0.0261	0.0054	—

phase, and vice-versa, will be associated with a substantial increase in the configurational energy of the system. For an initial slope defined by $b = 2(J^{[1]} - 2J^{[2]} + 3J^{[3]})$, and a configurational entropy defined by $\Delta S_f = -R[x_{\text{Ru}} \ln x_{\text{Ru}} + (1 - x_{\text{Ru}}) \ln(1 - x_{\text{Ru}})]$, the composition at the minimum of the free energy, $\Delta G_f = \Delta E_f - T\Delta S_f$, can be approximated by:

$$x_{\text{Ru}} = \frac{\exp(-b/k_B T)}{1 + \exp(-b/k_B T)}, \quad (3)$$

where k_B is the Boltzmann constant ($8.617 \times 10^{-5} \text{ eV K}^{-1}$). Although the free energy minimum of a single phase is not an exact measure of the equilibrium composition of the two-phase system, it can serve as a useful approximation to the appropriate order of magnitude in cases for which the energy changes are fairly steep and the concentrations are small. At 1000 K, the Ru concentrations determined from Equation (3) for the PdTe and $\text{Pd}_{20}\text{Te}_7$ systems are $x_{\text{Ru}}^* = 7.14 \times 10^{-3}$ and 2.11×10^{-5} , respectively. Likewise, the Pd

concentration that minimizes the hcp-phase free energy is $x_{\text{Pd}}^* = 1.12 \times 10^{-3}$.

Although the Pd concentration predicted in the binary metallic phase is less than 1% for this model, it should be noted that we have excluded several aspects from that model for the sake of simplification and clarity of presentation. A full thermodynamic treatment of phase separation between hcp metal and palladium telluride is possible given the established models for the five-metal alloy [4,5,14,19] and for the Pd–Te phase diagram [24–26,38]. These models include a greater configurational entropy term from the disorder introduced by including all five noble metal elements, as well as non-configurational (i.e. vibrational and electronic) contributions to the free energy, all of which may act to increase the Pd solubility.

The 1% value of Pd solubility is estimated at 1000 K. We reiterate that this does not reflect only the solubility in a purely binary system, but rather the much greater thermodynamic stability of the palladium-telluride phase over other phases when Te is present. Put another way, if the choice is between an hcp Ru-rich phase and an fcc Pd-rich phase, the solubility of Pd will be quite high in the hcp phase, but when the choice is between the hcp phase and a telluride phase, the Pd fractionation will favor the telluride phase instead until all of the available Te is exhausted. As noted, this 1% value is susceptible to changes when a model for the full 5-component alloy is introduced, along with new sources of entropy, but the experimental evidence demonstrates that it remains lower than the 5–10% composition commonly reported for the particle average.

With the observation of fractionation of Pd and Ru between the telluride and metallic phases, we turn to the question of a chemical mechanism to explain the formation of such NMP particles. The existence of a secondary phase raises the question of how and when that phase is formed and whether the constituent elements migrate to the particle nucleation site separately or concurrently. For example, Ru has been posited to diffuse to active sites as a gas-phase oxide molecule [10], but there is no corresponding molecule for PdO , which decomposes to O_2 and metallic Pd at high temperatures [48]. The Pd–Te system, by comparison, has a thermodynamically stable liquid phase with eutectic points at 505 °C and 780 °C occurring between 20 and 40 at.% Te [24]. As a result, tellurium is likely capable of acting as a carrier and mobile form for palladium, thereby enabling diffusion through the fuel matrix.

4. Conclusions

In this work, we have presented evidence, through both direct microscopy and first-principles thermodynamic calculations, for the presence of a Pd-rich telluride phase in particles that have previously been considered to contain only the noble metals. In the smallest particles, the fractionation of the Pd between the NMP and telluride phases is minor. This could be due to the phases overlapping with each other in the given field of view, or the extent of phase separation has not yet reached a high level. As particles get larger ($>100 \text{ nm}$), the Pd was observed to separate with preference to the telluride phase over the Ru-rich metallic phase.

Although a telluride phase has been shown to exist in some NMP particles, it is not necessarily guaranteed that such a phase will dominate the Pd fraction or even be present in every particle (though this was observed in every particle we analyzed with larger particles displaying a greater degree of phase separation). Depending on the atomic-scale mechanism for Pd migration, the fraction present in the metallic phase may vary from particle to particle and as a function of position within the fuel. Further work based on a broader statistical view of the distribution of particle

sizes and compositions within a larger section of the fuel will be necessary to obtain a clearer picture of the relative importance of the telluride phase in the formation, growth, and aggregation of NMP particles. Additionally, a modeling approach that takes into account the full range of compositions and possible telluride phases [5,26], applied at the narrow single-particle scale, can complement the experimental microscopic analysis to provide a useful model for predicting particle behavior in a broader range of fuel types and reactor conditions.

Because the catalytic activity of noble metals has been cited as a major controlling factor of the oxidation potential in nuclear waste repositories [12], the exact chemical state of the catalytically active elements is of interest for establishing the mechanism for reduction of H_2O_2 and dissolved actinides. Pd metal is a commonly used catalyst in many industrial applications and consequently a candidate species for this system. However, if the predominant Pd phase is a telluride, then the surface will have a drastically different configuration, and the metal centers are likely to have a slightly positive oxidation state. This electron deficiency in turn may affect surface binding of species of interest and determine whether Pd will participate in catalytic activity. Future studies will examine differences in these surface properties to ascertain more precisely how fractionation between phases could affect the overall activity of undissolved residue.

Author contributions

All authors have given approval to the final version of the manuscript.

CRediT authorship contribution statement

Sean H. Kessler: Conceptualization, Methodology, Software, Formal analysis, Writing - original draft, Visualization. **Timothy G. Lach:** Formal analysis, Investigation, Writing - review & editing. **Kerry E. Garrett:** Software, Methodology. **Michele A. Conroy:** Investigation. **David G. Abrecht:** Supervision. **Jon M. Schwantes:** Supervision, Funding acquisition. **Richard A. Clark:** Methodology, Writing - review & editing, Supervision, Project administration, Funding acquisition.

Declaration of competing interest

The authors declare that they have no known competing financial interests or personal relationships that could have appeared to influence the work reported in this paper.

Acknowledgements

This work was funded by Pacific Northwest National Laboratory utilizing Laboratory Directed Research and Development (LDRD) funds with support from the Nuclear Process Science Initiative (NPSI) and was performed using PNNL Institutional Computing (PIC). Microscopy experiments were performed in the PNNL RPL Facility within the RPL Microscopy Quiet Suite, which is outfitted with a FEI Helios 660 FIM/SEM and a JEOL GrandARM300 Aberration Corrected (AC) STEM/TEM. Additional TEM/STEM measurements were also collected on a JEOL ARM200 AC-STEM/TEM located in 3410, part of the Physical Sciences Facility. All of these instruments are part of PNNL's Institutional Microscopy Tools. Pacific Northwest National Laboratory is operated by Battelle Memorial Institute for the United States Department of Energy under contract DE-AC05-76RL0-1830.

Appendix A. Supplementary data

Supplementary data to this article can be found online at <https://doi.org/10.1016/j.jnucmat.2020.152249>.

References

- [1] J.I. Bramman, R.M. Sharpe, D. Thom, G. Yates, Metallic fission-product inclusions in irradiated oxide fuels, *J. Nucl. Mater.* 25 (1968) 201–215.
- [2] D. Cui, V.V. Rondinella, J.A. Fortner, A.J. Kropf, L. Eriksson, D.J. Wronkiewicz, K. Spahi, Characterization of alloy particles extracted from spent nuclear fuel, *J. Nucl. Mater.* 420 (2012) 328–333.
- [3] E.C. Buck, E.J. Mausolf, B.K. McNamara, C.Z. Soderquist, J.M. Schwantes, Nanostructure of metallic particles in light water reactor used nuclear fuel, *J. Nucl. Mater.* 461 (2015) 236–243.
- [4] S. Imoto, Chemical state of fission products in irradiated UO_2 , *J. Nucl. Mater.* 140 (1986) 19–27.
- [5] M.H. Kaye, B.J. Lewis, W.T. Thompson, Thermodynamic treatment of noble metal fission products in nuclear fuel, *J. Nucl. Mater.* 366 (2007) 8–27.
- [6] B.T. Bradbury, J.T. Demant, P.M. Martin, D.M. Poole, Electron probe microanalysis of irradiated UO_2 , *J. Nucl. Mater.* 17 (1965) 227–236.
- [7] R. Scheele, B. McNamara, A.M. Casella, A. Kozelisky, On the use of thermal NF_3 as the fluorination and oxidation agent in treatment of used nuclear fuels, *J. Nucl. Mater.* 424 (2012) 224–236.
- [8] D.J. Wronkiewicz, C.S. Watkins, A.C. Baughman, F.S. Miller, S.F. Wolf, Corrosion Testing of a Simulated Five-Metal Epsilon Particles in Spent Nuclear Fuel, 2002, pp. 625–632. Boston, MA.
- [9] S. Utsunomiya, R.C. Ewing, The fate of the epsilon phase (Mo-Ru-Pd-Tc-Rh) in the UO_2 of the Oklo natural fission reactors, *Radiochim. Acta* 94 (2006) 749–753.
- [10] H. Kleykamp, The chemical state of the fission products in oxide fuels, *J. Nucl. Mater.* 131 (1985) 221–246.
- [11] I.L.F. Ray, H. Thiele, H. Matzke, Transmission electron microscopy study of fission product behaviour in high burnup UO_2 , *J. Nucl. Mater.* 188 (1992) 90–95.
- [12] D. Cui, J. Low, V.V. Rondinella, K. Spahi, Hydrogen catalytic effects of nanostructured alloy particles in spent fuel on radionuclide immobilization, *Appl. Catal. B Environ.* 94 (2010) 173–178.
- [13] H. Kleykamp, Thermodynamics of the Mo-Ru system, *J. Less Common Met.* 144 (1988) 79–86.
- [14] H. Kleykamp, Constitution and thermodynamics of the Mo-Ru, Mo-Pd, Ru-Pd and Mo-Ru-Pd systems, *J. Nucl. Mater.* 167 (1989) 49–63.
- [15] L.A. Cornish, J.N. Pratt, Constitutional studies of the molybdenum-ruthenium-palladium ternary system, *J. Alloys Compd.* 247 (1997) 66–71.
- [16] A.E. Kissavos, S. Shallcross, V. Meded, L. Kaufman, I.A. Abrikosov, A critical test of ab initio and CALPHAD methods: the structural energy difference between bcc and hcp molybdenum, *Calphad* 29 (2005) 17–23.
- [17] A.E. Kissavos, S. Shallcross, L. Kaufman, O. Grånäs, A.V. Ruban, I.A. Abrikosov, Thermodynamics of ordered and disordered phases in the binary Mo-Ru system, *Phys. Rev. B* 75 (2007) 184203.
- [18] S.C. Middleburgh, D.M. King, G.R. Lumpkin, Atomic scale modelling of hexagonal structured metallic fission product alloys, *R. Soc. open sci.* 2 (2015) 140292.
- [19] S. Gossé, N. Dupin, C. Guéneau, J.-C. Crivello, J.-M. Joubert, Thermodynamic assessment of the Pd-Rh-Ru system using calphad and first-principles methods, *J. Nucl. Mater.* 474 (2016) 163–173.
- [20] S.H. Kessler, D.G. Abrecht, R.A. Clark, J.M. Schwantes, Vibrational contributions to phase stability in the Mo-Ru system, *J. Alloys Compd.* 689 (2016) 969–976.
- [21] D.J.M. King, P.A. Burr, E.G. Obbard, S.C. Middleburgh, DFT study of the hexagonal high-entropy alloy fission product system, *J. Nucl. Mater.* 488 (2017) 70–74.
- [22] K.L. Pellegrini, C.Z. Soderquist, S.D. Shen, E.J. Krogstad, C.J. Palmer, K.R. Gerez, E.C. Buck, T.G. Lach, J.M. Schwantes, R.A. Clark, Chemical and isotopic characterization of noble metal phase from commercial UO_2 fuel, *Anal. Chem.* 91 (2019) 6522–6529.
- [23] H. Kleykamp, J.O. Paschoal, R. Pejisa, F. Thümmel, Composition and structure of fission product precipitates in irradiated oxide fuels: correlation with phase studies in the Mo-Ru-Rh-Pd and BaO- UO_2 - ZrO_2 - MoO_2 Systems, *J. Nucl. Mater.* 130 (1985) 426–433.
- [24] G. Chattopadhyay, Y.J. Bhatt, S.K. Khara, Phase diagram of the Pd-Te system, *J. Less Common Met.* 123 (1986) 251–266.
- [25] M. Kelm, A. Görtzen, H. Kleykamp, H. Penthinghaus, On the constitution of the Pd-Te system up to 28 at.% Te, *J. Less Common Met.* 166 (1990) 125–133.
- [26] S. Gossé, C. Guéneau, Thermodynamic assessment of the palladium-tellurium (Pd-Te) system, *Intermetallics* 19 (2011) 621–629.
- [27] D. Cui, J. Low, C.J. Sjoestedt, K. Spahi, On Mo-Ru-Tc-Pd-Rh-Te alloy particles extracted from spent fuel and their leaching behavior under Ar and H_2 atmospheres, *Radiochim. Acta* 92 (2004) 551–554.
- [28] S.F. Wolf, D.L. Bowers, J.C. Cunnane, Analysis of high burnup spent nuclear fuel by ICP-MS, *J. Radioanal. Nucl. Chem.* 263 (2005) 581–586.
- [29] R.A. Clark, M.A. Conroy, T.G. Lach, E.C. Buck, K.L. Pellegrini, B.K. McNamara, J.M. Schwantes, Distribution of metallic fission-product particles in the cladding liner of spent nuclear fuel, *npj Mater. Degrad.* 4 (2020) 1–9.

- [30] B. Myers, TEM Sample Preparation with the FIB/SEM, NUANCE Center, Northwestern University, 2009.
- [31] T.G. Lach, D.J. Edwards, E.C. Buck, B.K. McNamara, J.M. Schwantes, R.A. Clark, Fission recoil-induced microstructural evolution of the fuel-cladding interface [FCI] in high burnup BWR fuel, *J. Nucl. Mater.* 521 (2019) 120–125.
- [32] J.M. Schwantes, J.L. Bair, E.C. Buck, R. Devanathan, S.H. Kessler, T.G. Lach, J.M. Loneragan, B.K. McNamara, C.J. Palmer, R.A. Clark, A new non-diffusional gas bubble production route in used nuclear fuel: Implications for fission gas release, cladding corrosion and next generation fuel design, *Phys. Chem. Chem. Phys.* 22 (2020) 6086–6099.
- [33] J.W.D. Connolly, A.R. Williams, Density-functional theory applied to phase transformations in transition-metal alloys, *Phys. Rev. B* 27 (1983) 5169–5172.
- [34] J.M. Sanchez, Cluster expansions and the configurational energy of alloys, *Phys. Rev. B* 48 (1993) 14013–14015.
- [35] A. van de Walle, M. Asta, G. Ceder, The alloy theoretic automated toolkit: a user guide, *Calphad* 26 (2002) 539–553.
- [36] A. van de Walle, G. Ceder, Automating first-principles phase diagram calculations, *J. Phase Equil.* 23 (2002) 348–359.
- [37] A. van de Walle, Multicomponent multisublattice alloys, nonconfigurational entropy and other additions to the Alloy Theoretic Automated Toolkit, *Calphad* 33 (2009) 266–278.
- [38] A. Kjekshus, W.B. Pearson, Constitution and magnetic and electrical properties of palladium tellurides (PdTe–PdTe₂), *Can. J. Phys.* 43 (1965) 438–449.
- [39] W. Wopersnow, K. Schubert, Kristallstruktur von Pd₂₀Sb₇ und Pd₂₀Te₇, *J. Less Common Met.* 62 (1977) 35–44.
- [40] G. Kresse, J. Furthmüller, Efficient iterative schemes for ab initio total-energy calculations using a plane-wave basis set, *Phys. Rev. B* 54 (1996) 11169–11186.
- [41] G. Kresse, J. Furthmüller, Efficiency of ab-initio total energy calculations for metals and semiconductors using a plane-wave basis set, *Comput. Mater. Sci.* 6 (1996) 15–50.
- [42] P.E. Blöchl, Projector augmented-wave method, *Phys. Rev. B* 50 (1994) 17953–17979.
- [43] J.P. Perdew, K. Burke, M. Ernzerhof, Generalized gradient approximation made simple, *Phys. Rev. Lett.* 77 (1996) 3865–3868.
- [44] H.J. Monkhorst, J.D. Pack, Special points for Brillouin-zone integrations, *Phys. Rev. B* 13 (1976) 5188–5192.
- [45] A. van de Walle, G. Ceder, The effect of lattice vibrations on substitutional alloy thermodynamics, *Rev. Mod. Phys.* 74 (2002) 11–45.
- [46] R.J. Parrish, K.E. Wright, A.J. Winston, C. McKinney, J.M. Harp, A. Aitkaliyeva, Characterization of solid fission products in 13.7% FIMA MOX fuel using electron microscopy techniques, *J. Nucl. Mater.* 524 (2019) 67–79.
- [47] T.F. Kelly, M.K. Miller, Atom probe tomography, *Rev. Sci. Instrum.* 78 (2007), 031101.
- [48] H. Zhang, J. Gromek, G.W. Fernando, S. Boorse, H.L. Marcus, PdO/Pd system equilibrium phase diagram under a gas mixture of oxygen and nitrogen, *J. Phase Equil.* 23 (2002) 246–248.